

# RLPR: Radar-to-LiDAR Place Recognition via Two-Stage Asymmetric Cross-Modal Alignment for Autonomous Driving

Zhangshuo Qi<sup>1</sup>, Jingyi Xu<sup>2</sup>, Luqi Cheng<sup>1</sup>, Shichen Wen<sup>1</sup>, Guangming Xiong<sup>\*</sup>

**Abstract**—All-weather autonomy is critical for autonomous driving, which necessitates reliable localization across diverse scenarios. While LiDAR place recognition is widely deployed for this task, its performance degrades in adverse weather. Conversely, radar-based methods, though weather-resilient, are hindered by the general unavailability of radar maps. To bridge this gap, radar-to-LiDAR place recognition, which localizes radar scans within existing LiDAR maps, has garnered increasing interest. However, extracting discriminative and generalizable features shared between modalities remains challenging, compounded by the scarcity of large-scale paired training data and the signal heterogeneity across radar types. In this work, we propose RLPR, a robust radar-to-LiDAR place recognition framework compatible with single-chip, scanning, and 4D radars. We first design a dual-stream network to extract structural features that abstract away from sensor-specific signal properties (e.g., Doppler or RCS). Subsequently, motivated by our task-specific asymmetry observation between radar and LiDAR, we introduce a two-stage asymmetric cross-modal alignment (TACMA) strategy, which leverages the pre-trained radar branch as a discriminative anchor to guide the alignment process. Experiments on four datasets demonstrate that RLPR achieves state-of-the-art recognition accuracy with strong zero-shot generalization capabilities.

## I. INTRODUCTION

In autonomous driving, all-weather localization is crucial for ensuring operational safety. Given the widespread availability of LiDAR maps, LiDAR place recognition (LPR) has matured into a de facto standard for global localization in GPS-denied environments [1], [2], [3], [4], typically by matching online query scans against a pre-built database. However, this paradigm lacks robustness in adverse weather [5], [6], where signal interference and attenuation induced by fog or snow significantly degrade the accuracy of LPR. In contrast, radar serves as an ideal candidate for all-weather localization due to its signal penetration and cost-effectiveness [7], [8], [9]. Nonetheless, the scarcity of large-scale radar maps makes constructing comprehensive databases for radar place recognition (RPR) challenging. Consequently, radar-to-LiDAR (R2L) place recognition has emerged as a practical alternative [10], [11], enabling the localization of radar queries within existing LiDAR databases.

This work was supported by the National Natural Science Foundation of China under Grant 52372404.

<sup>1</sup>Zhangshuo Qi, Luqi Cheng, Shichen Wen and Guangming Xiong are with Beijing Institute of Technology (xiongguangming@bit.edu.cn).

<sup>2</sup>Jingyi Xu is with Shanghai Jiao Tong University.

\*Corresponding author: Guangming Xiong

Our open-source code will be available at <https://github.com/QiZS-BIT/RLPR>.

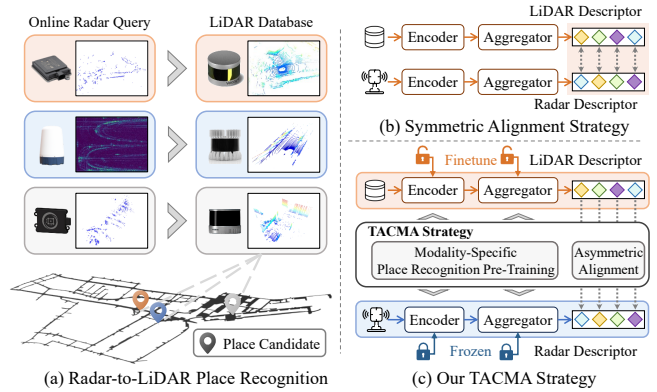


Fig. 1: Conceptual overview of the proposed RLPR framework. (a) RLPR facilitates robust place recognition across heterogeneous radar types. (b) Existing methods perform symmetric feature alignment. (c) Motivated by the task-specific asymmetry between radar and LiDAR, we design a two-stage asymmetric cross-modal alignment (TACMA) strategy that enables effective feature alignment.

Despite its potential, the practical deployment of R2L methods is hindered by the substantial cross-modal gap between these two sensing modalities. Specifically, several critical challenges remain to be solved: (1) Existing R2L methods are primarily tailored for dense scanning radar, often relying on temporally accumulated LiDAR scans to approximate the distribution of a radar frame [10], [11]. However, as single-chip and 4D radars become increasingly prevalent, an R2L framework capable of handling these diverse radar types remains underexplored. (2) Current R2L approaches typically enforce feature alignment within a shared latent space. However, this paradigm often overlooks the preservation of intra-modal discriminability while simultaneously underestimating the intrinsic heterogeneity of different modalities. Given the relative scarcity of paired radar-LiDAR training data, such forced alignment struggles to learn sufficiently generalizable representations.

To address these challenges, we propose RLPR, a radar-to-LiDAR place recognition framework compatible with heterogeneous radar types. To overcome radar format discrepancies, we design a polar bird’s-eye view (BEV) dual-stream network. This network abstracts away modality-specific physical signatures, focusing exclusively on extracting hierarchical structural features. Furthermore, we re-examine the symmetric alignment paradigm by revealing a task-driven asymmetry between the two modalities. While raw LiDAR data are inherently richer in spatial detail, our observation shows that the radar features naturally evolve toward a higher-entropy representation for intra-modal discriminability. Consequently, aligning these structurally rigid

and information-dense radar representations with compact LiDAR features risks degrading geometric cues and destabilizing optimization. Motivated by this, we propose a two-stage asymmetric cross-modal alignment (TACMA) strategy, as shown in Fig. 1. Following independent pre-training for modality-specific discriminability, we freeze the radar branch as an anchor in the asymmetric alignment stage. This strategy streamlines feature alignment along a more tractable path while anchoring the shared latent space onto a discriminative manifold, ensuring precise cross-modal retrieval with minimal unimodal discriminability loss.

In summary, our main contributions are as follows:

- We propose RLPR, a radar-to-LiDAR place recognition framework compatible with heterogeneous radar types.
- We introduce a two-stage asymmetric cross-modal alignment strategy to harmonize LiDAR and radar features while minimizing the sacrifice of unimodal discriminability.
- Extensive evaluations across four datasets demonstrate that RLPR achieves accurate and generalizable R2L place recognition, while exhibiting significant robustness in adverse weather conditions.

## II. RELATED WORK

### A. LiDAR and Radar Place Recognition

The widespread adoption of LiDAR maps in autonomous driving has catalyzed significant progress in LiDAR place recognition (LPR) [3], [4], [12], [13]. We recommend referring to [14] for a comprehensive survey. Despite their precision, LiDARs are prone to signal attenuation and noise in adverse weather conditions, leading to performance degradation in LPR systems [5], [6].

In contrast, the inherent robustness of radar has sparked increasing interest in radar place recognition (RPR). Many existing methods have primarily leveraged scanning radars for their relatively dense and accurate nature. For example, KidnappedRadar [15] learns to extract rotation-invariant features, while ReFeree [16] utilizes statistical methods for lightweight descriptor generation. RaPlace [17] employs the Radon transform for robust representations, and OpenRadVLAD [8] operates at the radial frequencies for feature clustering. However, scanning radars are often constrained by their hardware cost and physical footprint, which limits their adoption in autonomous vehicles. While single-chip radars offer a more deployable alternative, they present greater challenges due to their inherent data sparsity and noise. To achieve robust RPR for single-chip radars, AutoPlace [7] incorporates a temporal feature accumulation strategy. SPR [18] integrates RCS features to improve recognition accuracy. More recently, the emergence of 4D imaging radars has introduced elevation resolution, offering promising prospects. TransLoc4D [9] uses sparse convolutions for feature extraction, and 4D RadarPR [19] validates the robustness of 4D RPR in harsh scenarios.

Despite these strides, the practical utility of RPR remains constrained by the lack of extensive radar databases [11].

Leveraging the widespread availability of LiDAR-based infrastructure, cross-modal place recognition has emerged as a pragmatic paradigm for all-weather localization.

### B. Cross-Modal Place Recognition

Cross-modal place recognition primarily evolved from camera-to-LiDAR (C2L) matching, which focuses on bridging the gap between textural and structural information. Cattaneo et al. [20] laid the foundation for this field by proposing a composite loss strategy to symmetrically align 2D image and 3D point cloud features in a shared latent space. To mitigate the inherent modality gap, subsequent studies have explored projecting 3D point clouds into range images prior to alignment. For instance, ModaLink [21] utilizes triplet loss for feature alignment between RGB and range images, LIP-Loc [22] adopts a contrastive learning paradigm, and I2P-CMPR [23] further captures 2D cross-modal correspondences at both global and local scales.

Drawing inspiration from the C2L paradigm, existing radar-to-LiDAR (R2L) place recognition methods predominantly adopt a symmetric alignment strategy. Radar-to-LiDAR [10] pioneered this field by exploring cross-modal matching between scanning radar images and LiDAR map projections, while RaLF [11] attempts to improve generalization by scaling up the training corpus of the place recognition module. Moving beyond existing R2L methods designed specifically for scanning radars, in this work, we extend R2L capability to accommodate various radar types, including single-chip and 4D radars. Furthermore, motivated by our task-specific asymmetry observation, we introduce the TACMA strategy, which enables accurate and generalizable R2L place recognition.

## III. OUR APPROACH

### A. System Overview

Given a query radar frame and a database consisting of LiDAR scans, our objective is to retrieve the most similar LiDAR scan corresponding to the same place. The core challenge of R2L place recognition lies in identifying cross-modal commonalities to bridge the domain gap. To this end, we propose RLPR, the overall pipeline of which is illustrated in Fig. 2. In light of the inherent asymmetry and discriminability of different modalities, we design a dual-stream architecture with identical configurations but independent parameter spaces. Data from different modalities are first projected into polar BEV format to serve as input. Before entering the backbone, these representations are processed by the proposed Polar Context Enhancer (PCE) module to filter noise and bridge modality discrepancies. The backbone then extracts geometric features from the refined representations, which are subsequently aggregated into dual-descriptors to capture both global context and local details. Finally, the two branches of the network are aligned through our proposed two-stage asymmetric cross-modal alignment (TACMA) strategy. We first leverage place recognition pre-training to establish intra-modal discriminability, followed

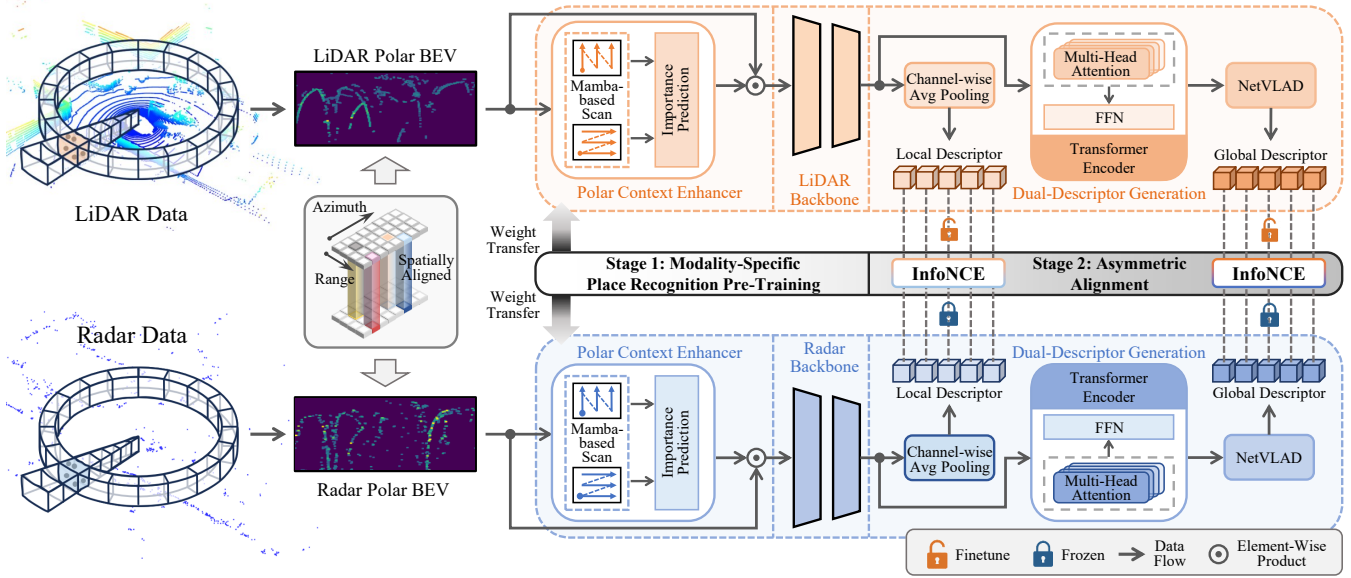


Fig. 2: The system overview of RLPR. The proposed radar-to-LiDAR place recognition framework consists of a dual-stream network and the two-stage asymmetric cross-modal alignment (TACMA) strategy. The dual-stream network is designed to extract global and local geometric features, while the TACMA strategy exploits cross-modal commonalities for accurate and generalizable retrieval.

by an asymmetric alignment stage where the radar branch serves as an anchor to uncover generalizable commonalities.

### B. Network Architecture

**Polar BEV Representation:** RLPR exploits the widely-recognized polar BEV representation [5], [8], [10] as a viewpoint robust data foundation for cross-modal place recognition. Given a point cloud  $\mathcal{P}$  from either LiDAR or radar, we discretize the 3D space into a 2D polar grid  $\mathcal{B}$ . Specifically, each point  $p_i = (x_i, y_i, z_i)^T$  in the point cloud  $\mathcal{P}$  is mapped to the pixel coordinates  $(u_i, v_i)$  of  $\mathcal{B}$  by:

$$\begin{pmatrix} u_i \\ v_i \end{pmatrix} = \begin{pmatrix} \frac{1}{2} [1 - \pi^{-1} \arctan(y_i, x_i)] w \\ [m^{-1} \sqrt{x_i^2 + y_i^2}] h \end{pmatrix} \quad (1)$$

where  $h$  and  $w$  represent the width and height of the polar BEV  $\mathcal{B}$ , and  $m$  is a predefined maximum perception range. The value at position  $(u_i, v_i)$  corresponds to the number of points falling within the corresponding grid cell. Notably, the polar representation naturally accommodates the horizontal field-of-view (FoV) variations. For radars with limited FoV, we adjust the mapping parameters accordingly to concentrate on a azimuthal sub-region, thereby preserving the high-fidelity structural details. By mapping raw data into this unified format, we effectively abstract away modality-specific physical signatures, preserving only the geometric structure. This establishes a common ground that enhances compatibility across radar types.

**Polar Context Enhancer:** While polar BEV offers a robust representation for place recognition, it inevitably inherits the noise in the raw radar measurements. To mitigate this, RLPR incorporates a lightweight Mamba-based enhancer to gate the input, thereby suppressing the noise-prone regions and refining the BEVs prior to the backbone.

The core of the enhancer is the discrete-time State Space Model (SSM), which maps an input sequence to an output

through a hidden state, as detailed in [24]. While standard SSMS are designed for modeling 1D sequences, the polar BEV  $\mathcal{B}$  exhibits a structured geometric topology along the range and azimuth axes. To capture global dependencies across these axes, we introduce a two-way scanning strategy. Specifically, after patchifying the polar BEV  $\mathcal{B}$  as  $\mathcal{B}_{\text{patch}} \in \mathbb{R}^{H \times W \times C}$ , we construct two mutually orthogonal input sequences  $s_{\text{rng}} \in \mathbb{R}^{(H \cdot W) \times C}$  and  $s_{\text{azi}} \in \mathbb{R}^{(W \cdot H) \times C}$  to traverse the grid. The sequences are then processed by the Mamba layer to aggregate dependencies along both axes. For computational efficiency, we propose using the modified Mamba implementation from [25], which exploits bidirectional context through non-causal convolutions, precluding the need for separate backward scans.

Finally, the features are concatenated and passed through 2D convolutions followed by a sigmoid activation to produce the importance map, as illustrated in Fig. 3. This map gates the polar BEV via element-wise multiplication, suppressing detrimental noise and boosting retrieval performance (see Tab. VII). Furthermore, for the cleaner LiDAR branch, the PCE module ensures latent-space consistency across modalities, and serves to attenuate the domain gap between disparate representations in the alignment process.

**Dual-Descriptor Generation:** After processing via the PCE module and a modality-specific backbone consisting of two ResBlocks [26], the polar BEV  $\mathcal{B}$  is compressed into a feature map  $\mathcal{F} \in \mathbb{R}^{H' \times W' \times C'}$ , which encodes essential geometric structures. The dual-descriptor generation process then aggregates the geometric information at both local and global levels. As detailed in Sec. IV-D, robust cross-modal alignment benefits significantly from the synergy between local geometric consistency and holistic scene context.

To preserve fine-grained geometric details, we apply channel-wise average pooling (CAP) to the feature map  $\mathcal{F}$ , followed by a linear transformation, to generate a local

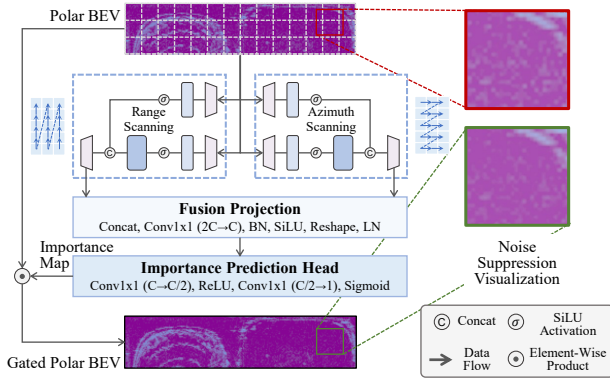


Fig. 3: Architecture of the proposed Polar Context Enhancer. It captures global dependencies through two-way scanning along range and azimuth axes, generating an importance map to gate the polar BEV. The corresponding images share the same color scale. descriptor  $\mathcal{D}_{loc} \in \mathbb{R}^D$ . We aim to employ CAP to encode spatial information while providing more consistent supervision for the cross-modal alignment process, thereby enhancing recognition accuracy, as shown in Tab. VII.

To capture the holistic context, we employ a transformer encoder [27] to process the feature map. The self-attention mechanism can be formulated as:

$$\text{Attention}(\mathcal{Q}, \mathcal{K}, \mathcal{V}) = \text{softmax} \left( \frac{\mathcal{Q}\mathcal{K}^T}{\sqrt{d_k}} \right) \mathcal{V} \quad (2)$$

where  $\mathcal{Q}, \mathcal{K}, \mathcal{V}$  are linear projections of the feature map  $\mathcal{F}$ , representing queries, keys, and values, respectively, and  $d_k$  is the channel dimension. Following the transformer encoder, a NetVLAD [28] layer is employed to aggregate the context into the global descriptor  $\mathcal{D}_{glob} \in \mathbb{R}^D$ . Finally,  $\mathcal{D}_{loc}$  and  $\mathcal{D}_{glob}$  are concatenated as  $\mathcal{D} \in \mathbb{R}^{2D}$  for cross-modal retrieval.

### C. Two-Stage Cross-Modal Alignment

#### Modality-Specific Place Recognition Pre-Training:

Given the proposed network architecture, the efficacy of R2L retrieval hinges on the seamless alignment of disparate feature manifolds. However, we observe that directly enforcing cross-modal alignment from initial weights, or through simultaneous joint optimization, often leads to suboptimal results (see Tab. IV). We attribute this to a “cold-start” effect, where the network struggles to extract discriminative intra-modal features for place retrieval, thereby making the discovery of cross-modal correspondences ill-posed.

To address this, we decouple the learning process into a two-stage strategy that prioritizes intra-modal discriminability prior to cross-modal alignment. In the first stage, both branches are independently pre-trained to extract stable and discriminative features. Following the established practice in LPR [4], [5], [12], we employ the lazy triplet loss [1] for place recognition pre-training. Taking the radar branch as an example, for a given query descriptor  $\mathcal{D}_q^{ra}$ , we randomly sample a positive sample  $\mathcal{D}_{pos}^{ra}$  and select  $J$  hard negatives  $\{\mathcal{D}_{neg,j}^{ra}\}_{j=1}^J$  via hard negative mining to form a triplet. The lazy triplet loss  $\mathcal{L}_{LT}$  is then formulated as:

$$\mathcal{L}_{LT} = \left[ \alpha + d(\mathcal{D}_q^{ra}, \mathcal{D}_{pos}^{ra}) - \max_j (d(\mathcal{D}_q^{ra}, \{\mathcal{D}_{neg,j}^{ra}\}_{j=1}^J)) \right]_+ \quad (3)$$

where  $[\cdot]_+$  denotes the hinge loss,  $d(\cdot)$  means the Euclidean distance, and  $\alpha$  is the predefined margin. The LiDAR branch is trained following the same procedure. This stage ensures that each branch acquires a robust intra-modal retrieval capability, providing a well-conditioned initialization for the subsequent discovery of cross-modal commonalities.

**The Task-Specific Asymmetry Observation:** To determine an optimal alignment paradigm for the pre-trained features, we employ conditional entropy as a proxy for measuring their global information-sharing characteristics. We treat the polar BEV feature maps  $\mathcal{F}^{li}$  and  $\mathcal{F}^{ra}$ , extracted by the convolutional backbones, as random variables  $L$  and  $R$ , respectively. By discretizing the feature space into  $B$  bins, we estimate the joint probability distribution  $P(L, R)$  and  $P(R, L)$  via normalized 2D histograms. The conditional entropy  $H(L|R)$  and  $H(R|L)$  is defined as:

$$H(L|R) = - \sum_{r \in \mathcal{X}_R} \sum_{l \in \mathcal{X}_L} P(l, r) \log \frac{P(l, r)}{P(r)} \quad (4)$$

$$H(R|L) = - \sum_{l \in \mathcal{X}_L} \sum_{r \in \mathcal{X}_R} P(l, r) \log \frac{P(l, r)}{P(l)} \quad (5)$$

where  $l \in \mathcal{X}_L$  and  $r \in \mathcal{X}_R$  denote the specific realizations within their respective discretized feature spaces,  $P(l, r)$  represents the joint probability of the features co-occurring in specific bins, while  $P(r)$  and  $P(l)$  are the marginal probability of radar and LiDAR features, respectively.

For each radar type, we compute the mean  $H(L|R)$  and  $H(R|L)$  across all corresponding splits (see Sec. IV-A) to obtain representative estimates. As illustrated in Fig. 4, our empirical analysis reveals that while  $H(L|R)$  generally exceeds  $H(R|L)$  in an initial state, this relationship consistently reverses after modality-specific pre-training. Even for the 4D radar, which starts with an initial  $H(L|R) < H(R|L)$ , this relationship persists throughout pre-training and ultimately aligns with the trends observed in other radar types. This phenomenon is intrinsically linked to the evolution of marginal entropy  $H(L)$  and  $H(R)$ . Initially,  $H(L) > H(R)$  reflects the structural richness inherent in raw LiDAR data. However, following modality-specific pre-training, the radar features evolve a counter-intuitively higher entropy compared to LiDAR (see Fig. 4). These results indicate that radar’s inherent properties necessitate a high-entropy manifold for place recognition, where forced alignment of such structurally rigid and fragile representations risks significant optimization bottlenecks and potential information loss. In contrast, LiDAR’s representational redundancy allows it to accommodate increased complexity while preserving its discriminability. The evidence supporting this inference is further detailed in Tab. VI. Consequently, designating radar features as the alignment anchor not only facilitates a more tractable optimization path but also precludes potential representational manifold collapse.

**Asymmetric Alignment:** Motivated by the task-specific asymmetry observations, we perform asymmetric alignment on the pre-trained features. Specifically, we designate the radar branch as a frozen feature anchor and the LiDAR

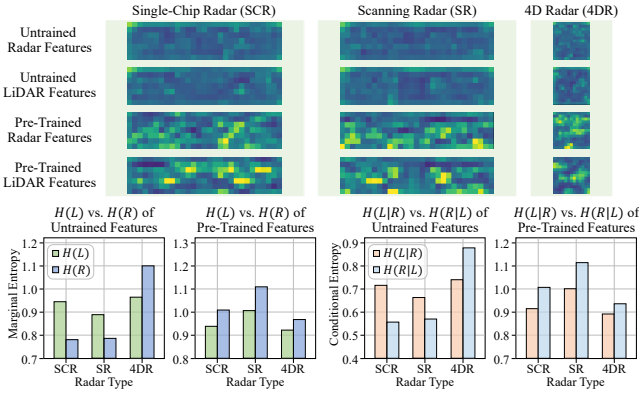


Fig. 4: Conditional entropy analysis and feature map visualizations. A comparison of the feature maps shows that pre-training enables the extraction of distinct geometric saliency. Meanwhile, the intrinsic asymmetry between LiDAR and Radar drives a divergence in marginal entropy after pre-training, which leads to the observed reversal in conditional entropy. All visualizations are channel-averaged and share the same color scale.

branch as a trainable student, and utilize the asymmetric InfoNCE loss [29] to align both local and global descriptors. This process is formulated as:

$$\mathcal{L}_{\text{INI}} = -\frac{1}{N} \sum_{a=1}^N \log \frac{\exp(\{\mathcal{D}_{\text{loc}}^{\text{ra}}\}_a \cdot \{\mathcal{D}_{\text{loc}}^{\text{li}}\}_a / \tau)}{\sum_{b=1}^N \exp(\{\mathcal{D}_{\text{loc}}^{\text{ra}}\}_a \cdot \{\mathcal{D}_{\text{loc}}^{\text{li}}\}_b / \tau)} \quad (6)$$

$$\mathcal{L}_{\text{Ing}} = -\frac{1}{N} \sum_{a=1}^N \log \frac{\exp(\{\mathcal{D}_{\text{glob}}^{\text{ra}}\}_a \cdot \{\mathcal{D}_{\text{glob}}^{\text{li}}\}_a / \tau)}{\sum_{b=1}^N \exp(\{\mathcal{D}_{\text{glob}}^{\text{ra}}\}_a \cdot \{\mathcal{D}_{\text{glob}}^{\text{li}}\}_b / \tau)} \quad (7)$$

where  $\{\mathcal{D}_{\text{loc}}^{\text{ra}}\}$ ,  $\{\mathcal{D}_{\text{loc}}^{\text{li}}\}$ ,  $\{\mathcal{D}_{\text{glob}}^{\text{ra}}\}$ ,  $\{\mathcal{D}_{\text{glob}}^{\text{li}}\}$  denote batches of descriptors,  $N$  represents the batch size, and  $\tau$  is a predefined temperature parameter. Furthermore, we observe that asymmetric alignment generally outperforms joint fine-tuning of both branches (see Tab. V). This superiority is attributed to the establishment of a discriminative anchor, which prevents the modalities from over-aligning into a shared latent space and thereby sacrificing task-specific saliency (see Tab. VI).

## IV. EXPERIMENTS

### A. Experimental Setup

**Datasets:** We evaluate the proposed framework across four public datasets featuring three distinct radar types, namely MulRan [30], Boreas [31], nuScenes [32], and Snail-Radar [33]. For scanning radar-to-LiDAR place recognition, we employ MulRan as the primary benchmark. We follow the data split from [5] but additionally include ‘KAIST 01’ and ‘KAIST 02’ in the training set. Furthermore, Boreas is employed for cross-dataset generalization evaluation across two scenarios: Bor-Clear (clear-to-clear) and Bor-Snowy (snowy-to-clear). Both scenarios share the ‘2020-12-18-13-44’ sequence as the database, while the query are ‘2021-09-14-20-00’ and ‘2021-01-26-11-22’, respectively. For single-chip radar-to-LiDAR evaluation, we adopt nuScenes with the data splits defined in [7], [5]. Finally, we benchmark 4D radar-to-LiDAR performance using Snail-Radar, following the data organizations of TransLoc4D [9] while excluding sequences not from autonomous driving scenarios.

**Implementation Details:** We set the size of both radar and LiDAR polar BEV to (225, 50) for real-time performance. For 4D radar, we crop the LiDAR point cloud accordingly to match the radar’s coverage, generating polar BEVs of size (100, 100). The maximum perception range  $m$  is fixed at 80 meters. Both  $\mathcal{D}_{\text{loc}}$  and  $\mathcal{D}_{\text{glob}}$  have a dimension of  $D = 256$ , resulting in the final descriptor of size  $1 \times 512$ . When computing the conditional entropy, we set  $B = 10$ . During the pre-training stage, we set the loss margin  $\alpha = 0.5$  and the number of negative samples  $J = 10$ . Samples within 9 meters are defined as positives, while those beyond 12 meters are negatives. For the asymmetric alignment stage, we employ a batch size  $N = 12$  and a temperature parameter  $\tau = 0.07$ . Both stages are optimized using the Adam optimizer with an initial learning rate of  $5 \times 10^{-5}$  and a 20% decay per epoch. Following [7], the retrieval is considered successful if the candidate falls within 9 meters of the query.

**Baselines:** To evaluate the efficacy of our proposed method, we compare it against a diverse set of baselines. Beyond the primary R2L place recognition methods, namely Radar-to-LiDAR [10] and RaLF [11], we further incorporate two broader categories of baselines for comprehensive evaluation. The first category involves training SOTA unimodal methods in a cross-modal setting, including BEVPlace++ [4] for LiDAR, AutoPlace [7] for single-chip radar, Kidnappe-dRadar [15] for scanning radar, and TransLoc4D [9] for 4D radar. These adapted models are denoted with a ‘-CM’ suffix. The second category comprises camera-to-LiDAR methods, which are migrated to the R2L task. We select LIP-Loc [22] and I2P-CMPR [23], for their architectural design for aligning RGB images with LiDAR range images is structurally analogous to our polar BEV alignment. All baselines are implemented using their respective open-source code and retrained on our data splits to ensure a rigorous comparison. For RaLF, we use its official pre-trained weights as it is specifically optimized for zero-shot generalization via multi-dataset joint training. Supplementary evaluations of unimodal retrieval and robustness under adverse weather also incorporate FFT-RadVLAD [8] and MinkLoc3Dv2 [12].

### B. Radar-to-LiDAR Place Recognition Evaluation

Following [7], [5], we report the average recall of the top-K candidates (AR@K) and max  $F_1$  score as primary metrics to evaluate cross-modal recognition accuracy.

We present the R2L recognition accuracy comparisons for scanning, single-chip, and 4D radar in Tab. I, Tab. II and Tab. III, respectively. Note that the sequences ‘Riverside’, ‘DCC’, ‘SON’, and ‘SQ’ represent intra-dataset generalization scenarios with no spatiotemporal overlap with the training set, while Bor-Clear serves as a benchmark for cross-dataset zero-shot generalization. Our proposed RLPR consistently outperforms the baselines, underscoring RLPR’s robustness across heterogeneous radar types. Notably, on the cross-dataset Bor-Clear sequence, RLPR exhibits superior zero-shot generalization capabilities compared to RaLF, even RaLF is trained on multi-dataset.

TABLE I  
SCANNING RADAR-TO-LiDAR PERFORMANCE ON MULRAN & BOREAS

Methods	MulRan-Riverside				MulRan-DCC				Bor-Clear			
	AR@1	AR@5	AR@10	max $F_1$	AR@1	AR@5	AR@10	max $F_1$	AR@1	AR@5	AR@10	max $F_1$
KidnappedRadar-CM [15]	5.452	12.94	20.30	0.1286	9.575	23.94	42.02	0.2222	0.6890	2.493	4.133	0.02755
BEVPlace++-CM [4]	2.668	10.21	16.94	0.05198	2.660	10.64	21.81	0.07207	0.6562	2.067	3.642	0.01377
LIP-Loc [22]	7.135	17.40	23.43	0.1024	9.574	26.06	39.36	0.4000	0.7532	2.636	4.759	0.005448
I2P-CMPR [23]	4.292	19.84	31.73	0.01497	5.851	21.81	31.38	0.08163	3.771	12.12	19.58	0.01304
Radar-to-LiDAR [10]	31.13	44.54	50.96	0.4748	12.77	24.47	32.98	0.2264	24.51	49.61	61.25	0.3938
RaLF [11]	30.10	38.92	45.88	0.5942	34.04	50.53	55.85	0.5224	73.85	81.56	85.37	0.8576
RLPR (ours)	<b>64.85</b>	<b>78.77</b>	<b>84.22</b>	<b>0.8057</b>	<b>55.32</b>	<b>73.94</b>	<b>82.98</b>	<b>0.7419</b>	<b>87.60</b>	<b>94.26</b>	<b>95.31</b>	<b>0.9469</b>

The best and secondary results are highlighted in **bold black** and underline respectively.

TABLE II  
SINGLE-CHIP RADAR-TO-LiDAR PERFORMANCE ON NUSCENES

Methods	BS				SON				SQ			
	AR@1	AR@5	AR@10	max $F_1$	AR@1	AR@5	AR@10	max $F_1$	AR@1	AR@5	AR@10	max $F_1$
AutoPlace-CM [7]	64.65	76.48	79.51	0.7890	0.9072	1.693	2.510	0.01822	0.4706	2.353	3.177	0.03540
BEVPlace++-CM [4]	1.380	5.087	8.333	0.07576	0.7557	3.023	5.441	0.04545	4.935	16.80	25.73	0.09524
LIP-Loc [22]	14.64	30.07	37.94	0.2615	2.328	8.620	14.18	0.07122	5.882	18.45	26.79	0.1681
I2P-CMPR [23]	12.31	26.17	34.45	0.2635	15.84	34.07	42.65	0.3192	18.45	38.43	48.06	0.3518
RLPR (ours)	<b>70.85</b>	<b>80.30</b>	<b>82.79</b>	<b>0.8907</b>	<b>59.31</b>	<b>77.42</b>	<b>83.07</b>	<b>0.7582</b>	<b>47.71</b>	<b>60.63</b>	<b>66.04</b>	<b>0.6893</b>

TABLE III  
4D RADAR-TO-LiDAR PERFORMANCE ON SNAIL-RADAR

Method	81r				
	AR@1	AR@5	AR@10	AR@20	max $F_1$
TransLoc4D-CM [9]	13.73	19.82	23.18	26.84	0.4015
BEVPlace++-CM [4]	0.4884	0.5215	0.5463	1.010	0.04369
LIP-Loc [22]	7.427	18.00	25.68	35.25	0.1319
I2P-CMPR [23]	16.26	17.51	18.57	24.58	0.4118
RLPR (ours)	<b>44.71</b>	<b>47.58</b>	<b>50.16</b>	<b>62.13</b>	<b>0.6304</b>

Furthermore, we evaluate the efficiency on the BS split. On a system equipped with an i7-14700KF CPU and an RTX 4060Ti GPU, our method achieves a descriptor extraction time of 2.88 ms and a top-1 retrieval time of 0.17 ms on average, demonstrating superior real-time performance.

### C. Unimodal Place Recognition Evaluation

To validate that our TACMA strategy effectively preserves the inherent discriminability of each modality, we evaluate the RPR and LPR accuracy of our network. We report the average AR@K across all evaluation sequences for each radar type, alongside the mean LPR performance on MulRan and Boreas. As illustrated in Fig. 5, our RPR performance not only surpasses R2L baselines, but also achieves comparable accuracy with specialized RPR methods. Furthermore, while the LiDAR branch exhibits a slight performance gap compared to SOTA LPR method BEVPlace++, it outperforms all R2L baselines. These results validate that under our strategy, both branches are effectively aligned without compromising their inherent discriminability.

### D. Ablation Studies

**Place Recognition Pre-Training:** We conduct an ablation study on the modality-specific place recognition pre-training. We compare our proposed framework against two variants: No Pre-training, which bypasses the pre-training stage, and Joint Optimization, which unimodal and cross-modal losses are optimized simultaneously. As shown in Tab. IV, the No Pre-training variant suffers from severe performance degradation, highlighting the necessity of establishing robust modality-specific feature extraction capabilities before

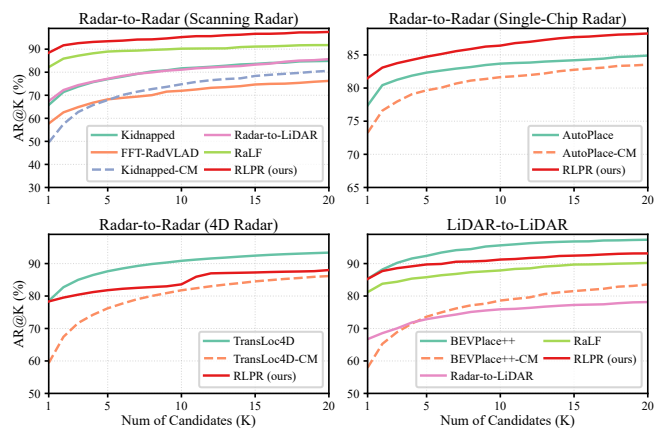


Fig. 5: A comparative visualization of radar-to-radar and LiDAR-to-LiDAR place recognition accuracy.

alignment. Furthermore, the suboptimal performance of the Joint Optimization variant indicates that premature cross-modal alignment risks convergence to a local minimum. This suggests that a two-stage alignment strategy is essential for maximizing both discriminability and alignment quality.

**Asymmetric Alignment:** We further conduct ablation study on the asymmetric alignment. Specifically, we benchmark three loss functions, including triplet, MSE, and InfoNCE. Each objective is tested under three settings: frozen LiDAR branch (Frozen L), joint fine-tuning of both branches (Both Trainable), and frozen radar branch (Frozen R). For the Both Trainable regime, symmetric versions of the Triplet and InfoNCE losses are employed for a fair comparison. As shown in Tab. V, the Frozen R configuration generally outperforms all other regimes across every loss variant, with the combination of InfoNCE and Frozen R producing the highest precision. This empirically corroborates the general applicability of our strategy, while validating the suitability of InfoNCE for exploiting cross-modal commonalities.

To elucidate our asymmetric alignment stage, we analyze the evolution of marginal entropy and modality-specific discriminability across different training regimes. As shown in Tab. VI, the stagnant entropy and unexpected RPR perfor-

TABLE IV  
ABLATION STUDY ON PLACE RECOGNITION PRE-TRAINING

Strategy	BS		SON		SQ		Riverside		DCC		Bor-Clear		81r	
	AR@1	AR@5												
No Pre-training	20.35	39.69	5.804	15.39	3.760	12.34	8.469	19.55	10.64	35.11	3.018	5.053	29.85	32.21
Joint Optimization	44.18	60.90	24.88	38.15	20.21	33.37	21.64	39.56	22.87	48.40	17.03	21.95	32.83	34.29
Modality-Specific Pre-Training	<b>70.85</b>	<b>80.30</b>	<b>59.31</b>	<b>77.42</b>	<b>47.71</b>	<b>60.63</b>	<b>64.85</b>	<b>78.77</b>	<b>55.32</b>	<b>73.94</b>	<b>87.60</b>	<b>94.26</b>	<b>44.71</b>	<b>47.58</b>

TABLE V  
ABLATION STUDY ON ALIGNMENT STRATEGY

Loss	Alignment Strategy	BS		SON		SQ		Riverside		DCC		Bor-Clear		81r	
		AR@1	AR@5												
Triplet	Frozen L	44.29	58.09	32.22	49.58	7.451	23.40	46.40	64.10	45.74	69.68	62.60	68.41	17.95	19.49
Triplet	Both Trainable	61.09	71.37	44.53	61.22	45.71	58.05	56.38	72.85	56.38	<b>78.72</b>	84.84	88.16	26.05	27.94
Triplet	Frozen R	55.89	66.90	37.88	58.52	44.18	56.64	59.05	75.00	55.32	75.00	84.71	88.19	23.45	25.05
MSE	Frozen L	60.08	71.18	27.81	42.50	39.84	56.05	56.61	71.29	39.89	66.49	46.10	52.76	30.67	32.60
MSE	Both Trainable	1.735	6.478	1.183	4.414	2.473	7.173	11.48	23.67	10.11	24.47	0.7218	2.067	1.349	1.606
MSE	Frozen R	68.43	77.30	57.89	74.24	46.77	59.11	62.88	77.90	<b>56.91</b>	75.53	80.94	89.90	43.10	45.94
InfoNCE	Frozen L	65.60	75.75	38.60	54.75	43.60	56.17	64.68	<b>80.34</b>	51.60	77.66	69.49	74.54	40.64	42.74
InfoNCE	Both Trainable	52.42	66.20	54.63	73.73	42.07	56.64	48.67	66.13	50.53	71.81	70.51	76.90	41.45	<b>49.66</b>
InfoNCE	Frozen R	<b>70.85</b>	<b>80.30</b>	<b>59.31</b>	<b>77.42</b>	<b>47.71</b>	<b>60.63</b>	<b>64.85</b>	78.77	55.32	73.94	<b>87.60</b>	<b>94.26</b>	<b>44.71</b>	47.58

TABLE VI  
THE IMPACT OF ALIGNMENT STRATEGIES ON MODALITY-SPECIFIC DISCRIMINABILITY

Alignment Strategy	Single-Chip Radar (On Average)				Scanning Radar (On Average)				4D Radar (On Average)			
	$H(L)$	$H(R)$	LPR (AR@1)	RPR (AR@1)	$H(L)$	$H(R)$	LPR (AR@1)	RPR (AR@1)	$H(L)$	$H(R)$	LPR (AR@1)	RPR (AR@1)
Pre-Alignment	0.9378	1.088	88.26	81.51	1.060	1.184	86.78	88.14	0.9213	0.9670	87.34	78.45
Frozen L	0.9378	1.114	88.26 (-0.00)	81.50 (-0.01)	1.060	1.182	86.78 (-0.00)	85.81 (-2.33)	0.9213	1.055	87.34 (-0.00)	73.10 (-5.35)
Both Trainable	1.215	1.112	81.82 (-6.44)	74.00 (-7.51)	1.110	1.103	79.58 (-7.20)	77.39 (-10.75)	1.097	0.9365	82.72 (-4.62)	76.91 (-1.54)
Frozen R	1.266	1.088	85.41 (-2.85)	81.51 (-0.00)	1.156	1.184	85.23 (-1.55)	88.14 (-0.00)	1.127	0.9670	83.70 (-3.64)	78.45 (-0.00)

TABLE VII  
ABLATION STUDY ON NETWORK ARCHITECTURE

CMP	LD	GD	PCE	BS		SON		SQ	
				AR@1	AR@5	AR@1	AR@5	AR@1	AR@5
$\times$	$\checkmark$	$\times$	$\times$	43.21	61.01	8.827	19.56	13.87	29.02
$\times$	$\times$	$\checkmark$	$\times$	51.00	69.07	9.341	23.49	14.57	33.96
$\times$	$\checkmark$	$\checkmark$	$\times$	64.26	75.70	55.17	71.70	44.07	56.29
$\checkmark$	$\checkmark$	$\checkmark$	$\checkmark$	68.21	78.33	49.03	67.71	43.60	56.05
$\times$	$\checkmark$	$\checkmark$	$\checkmark$	<b>70.85</b>	<b>80.30</b>	<b>59.31</b>	<b>77.42</b>	<b>47.71</b>	<b>60.63</b>

TABLE VIII  
COMPARISON OF PERFORMANCE IN SNOWY SCENARIO

Method	Bor-Snow				
	AR@1	AR@5	AR@10	AR@20	max $F_1$
MinkLoc3Dv2 [12]	18.83	31.63	37.45	43.49	0.4606
BEVPlace++ [4]	67.31	73.62	76.01	79.49	0.8524
Radar-to-LiDAR [10]	5.158	24.49	48.46	62.68	0.09880
RaLF [11]	74.79	86.81	90.65	93.88	0.8588
RLPR (ours)	<b>85.52</b>	<b>93.92</b>	<b>95.86</b>	<b>97.58</b>	<b>0.9226</b>

mance degradation under Frozen L reveal the structural rigidity of the radar manifold, and suggesting its high-entropy nature intrinsically embeds discriminability rather than mere sensor noise. This is further substantiated by the Frozen R regime, where LiDAR maintains high discriminability after aligning with radar features, indicating the latter provides a discriminative space rich in modality-specific cues. Consequently, forcing pre-trained radar features to conform to the LiDAR space not only fails to improve accuracy via denoising as expected, but also induces significant optimization bottlenecks and potential information loss. Moreover, LiDAR’s seamless adaptation to the high-entropy radar space not only highlights its inherent redundancy, but also show that Frozen R represents a more tractable optimization trajectory. This tractability is evidenced by the unconstrained Both Trainable regime, whose entropy trajectory naturally mirrors Frozen

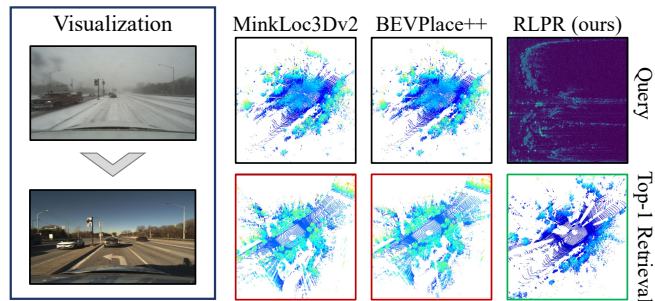


Fig. 6: Visualization of retrieval results in adverse weather. LPR methods are severely degraded by snow-induced noise, leading to consistent retrieval failures, whereas our proposed R2L method.

R. However, the Both Trainable regime suffers from severe task-specific saliency erosion, degrading unimodal and cross-modal performance. This discrepancy highlights the fragility of aligning with radar’s high-entropy distribution without a fixed discriminative anchor. Ultimately, Frozen R emerges as the optimal paradigm, offering a tractable optimization landscape while preserving task-specific discriminability.

**Network Architecture:** To validate the efficacy of our network design, we conduct an ablation study on the core components: the Local Descriptor (LD), Global Descriptor (GD), and Polar Context Enhancer (PCE). We also evaluate a variant replacing our default channel-wise average pooling (CAP) with channel-wise max pooling (CMP) for local descriptor aggregation. As detailed in Tab. VII, the LD-encoded local structure and the global geometric context captured by GD complement each other effectively, both being essential to ensure accuracy and generalization capability. The PCE further enhances accuracy by suppressing

noise and bridging the cross-modal domain gap. Finally, the performance degradation observed in the CMP variant justifies our adoption of CAP for local descriptor extraction.

### E. Robustness to Adverse Weather

In this section, we utilize the Bor-Snow sequence to quantitatively benchmark the robustness of R2L retrieval against LPR under adverse weather conditions. Notably, this sequence serves as a zero-shot sequence for all methods. As shown in Tab. VIII, SOTA LPR methods suffer severe performance degradation. This degradation stems from the heavy artifacts in LiDAR point clouds caused by snowfall, which lead to consistent failure patterns, as visualized in Fig. 6. In contrast, our proposed R2L framework demonstrates superior resilience, indicating the potential of R2L as a complementary method for robust localization in harsh environments.

## V. CONCLUSION

In this paper, we propose RLPR, a framework designed for radar-to-LiDAR place recognition across heterogeneous radar types. To address the inherent asymmetry between LiDAR and radar modalities in place recognition, we introduce the TACMA strategy that leverages pre-trained radar features as the discriminative anchor to exploit cross-modal geometric commonalities within polar BEV representations. Extensive experiments across four public datasets demonstrate that RLPR achieves SOTA R2L accuracy while preserving the discriminability of individual modalities, demonstrating its capability to serve as a solution for robust localization in all-weather environments.

## REFERENCES

- [1] M. A. Uy and G. H. Lee, "PointNetVLAD: Deep point cloud based retrieval for large-scale place recognition," in *Proceedings of the IEEE conference on computer vision and pattern recognition*, 2018, pp. 4470–4479.
- [2] X. Chen, T. Läbe, A. Milioto, T. Röhling, J. Behley, and C. Stachniss, "OverlapNet: A siamese network for computing LiDAR scan similarity with applications to loop closing and localization," *Autonomous Robots*, pp. 1–21, 2022.
- [3] J. Ma, J. Zhang, J. Xu, R. Ai, W. Gu, and X. Chen, "OverlapTransformer: An efficient and yaw-angle-invariant transformer network for LiDAR-based place recognition," *IEEE Robotics and Automation Letters*, vol. 7, no. 3, pp. 6958–6965, 2022.
- [4] L. Luo, S.-Y. Cao, X. Li, J. Xu, R. Ai, Z. Yu, and X. Chen, "BEVPlace++: Fast, robust, and lightweight lidar global localization for unmanned ground vehicles," *IEEE Transactions on Robotics (TRO)*, 2025.
- [5] Z. Qi, L. Cheng, Z. Zhou, and G. Xiong, "LRFusionPR: A polar BEV-based LiDAR-radar fusion network for place recognition," *IEEE Robotics and Automation Letters*, vol. 10, no. 11, pp. 11 784–11 791, 2025.
- [6] W. Kuang, X. Zhao, Y. Shen, C. Wen, H. Lu, Z. Zhou, and X. Chen, "ResLPR: A LiDAR data restoration network and benchmark for robust place recognition against weather corruptions," in *2025 IEEE/RSJ International Conference on Intelligent Robots and Systems (IROS)*, 2025, pp. 12 494–12 501.
- [7] K. Cait, B. Wang, and C. X. Lu, "AutoPlace: Robust place recognition with single-chip automotive radar," in *2022 International Conference on Robotics and Automation (ICRA)*. IEEE, 2022, pp. 2222–2228.
- [8] M. Gadd and P. Newman, "Open-RadVLAD: Fast and robust radar place recognition," in *2024 IEEE Radar Conference (RadarConf24)*. IEEE, 2024, pp. 1–6.
- [9] G. Peng, H. Li, Y. Zhao, J. Zhang, Z. Wu, P. Zheng, and D. Wang, "TransLoc4D: Transformer-based 4D radar place recognition," in *Proceedings of the IEEE/CVF Conference on Computer Vision and Pattern Recognition*, 2024, pp. 17 595–17 605.
- [10] H. Yin, X. Xu, Y. Wang, and R. Xiong, "Radar-to-Lidar: Heterogeneous place recognition via joint learning," *Frontiers in Robotics and AI*, vol. 8, p. 661199, 2021.
- [11] A. Nayak, D. Cattaneo, and A. Valada, "RaLF: Flow-based global and metric radar localization in LiDAR maps," in *2024 IEEE International Conference on Robotics and Automation (ICRA)*. IEEE, 2024, pp. 5097–5103.
- [12] J. Komorowski, "Improving point cloud based place recognition with ranking-based loss and large batch training," in *2022 26th international conference on pattern recognition (ICPR)*. IEEE, 2022, pp. 3699–3705.
- [13] J. Ma, G. Xiong, J. Xu, and X. Chen, "CVTNet: A cross-view transformer network for LiDAR-based place recognition in autonomous driving environments," *IEEE Transactions on Industrial Informatics*, 2023.
- [14] P. Yin, J. Jiao, S. Zhao, L. Xu, G. Huang, H. Choset, S. Scherer, and J. Han, "General place recognition survey: Toward real-world autonomy," *IEEE Transactions on Robotics*, vol. 41, pp. 3019–3038, 2025.
- [15] Ş. Săftescu, M. Gadd, D. De Martini, D. Barnes, and P. Newman, "Kidnapped Radar: Topological radar localisation using rotationally-invariant metric learning," in *2020 IEEE International Conference on Robotics and Automation (ICRA)*. IEEE, 2020, pp. 4358–4364.
- [16] H. Kim, B. Choi, E. Choi, and Y. Cho, "ReFeree: Radar-based lightweight and robust localization using feature and free space," *IEEE Robotics and Automation Letters*, 2024.
- [17] H. Jang, M. Jung, and A. Kim, "RaPlace: Place recognition for imaging radar using radon transform and mutable threshold," in *2023 IEEE/RSJ International Conference on Intelligent Robots and Systems (IROS)*. IEEE, 2023, pp. 11 194–11 201.
- [18] D. C. Herraes, L. Chang, M. Zeller, L. Wiesmann, J. Behley, M. Heidisfeld, and C. Stachniss, "SPR: Single-scan radar place recognition," *IEEE Robotics and Automation Letters*, 2024.
- [19] Y. Chen, Y. Zhuang, B. Wang, and J. Huai, "4D RadarPR: Context-aware 4d radar place recognition in harsh scenarios," *ISPRS Journal of Photogrammetry and Remote Sensing*, vol. 221, pp. 210–223, 2025.
- [20] D. Cattaneo, M. Vaghi, S. Fontana, A. L. Ballardini, and D. G. Sorrenti, "Global visual localization in LiDAR-maps through shared 2D-3D embedding space," in *2020 IEEE International Conference on Robotics and Automation (ICRA)*, 2020, pp. 4365–4371.
- [21] W. Xie, L. Luo, N. Ye, Y. Ren, S. Du, M. Wang, J. Xu, R. Ai, W. Gu, and X. Chen, "ModaLink: Unifying modalities for efficient image-to-pointcloud place recognition," in *2024 IEEE/RSJ International Conference on Intelligent Robots and Systems (IROS)*, 2024, pp. 3326–3333.
- [22] S. S. Puligilla, M. Omama, H. Zaidi, U. S. Parihar, and M. Krishna, "LIP-Loc: LiDAR image pretraining for cross-modal localization," in *2024 IEEE/CVF Winter Conference on Applications of Computer Vision Workshops (WACVW)*, 2024, pp. 939–948.
- [23] G. Yao, X. Li, L. Fu, and Y. Pan, "Monocular visual place recognition in LiDAR maps via cross-modal state space model and multi-view matching," in *2025 IEEE International Conference on Robotics and Automation (ICRA)*, 2025, pp. 2154–2161.
- [24] A. Gu and T. Dao, "Mamba: Linear-time sequence modeling with selective state spaces," *arXiv preprint arXiv:2312.00752*, 2024.
- [25] A. Hatamizadeh and J. Kautz, "MambaVision: A hybrid mamba-transformer vision backbone," in *Proceedings of the IEEE/CVF Conference on Computer Vision and Pattern Recognition (CVPR)*, June 2025, pp. 25 261–25 270.
- [26] K. He, X. Zhang, S. Ren, and J. Sun, "Deep residual learning for image recognition," in *Proceedings of the IEEE conference on computer vision and pattern recognition*, 2016, pp. 770–778.
- [27] A. Vaswani, "Attention is all you need," *Advances in Neural Information Processing Systems*, 2017.
- [28] R. Arandjelovic, P. Gronat, A. Torii, T. Pajdla, and J. Sivic, "NetVLAD: CNN architecture for weakly supervised place recognition," in *Proceedings of the IEEE conference on computer vision and pattern recognition*, 2016, pp. 5297–5307.
- [29] A. van den Oord, Y. Li, and O. Vinyals, "Representation learning with contrastive predictive coding," *arXiv preprint arXiv:1807.03748*, 2019.

- [30] G. Kim, Y. S. Park, Y. Cho, J. Jeong, and A. Kim, "MulRan: Multimodal range dataset for urban place recognition," in *2020 IEEE international conference on robotics and automation (ICRA)*. IEEE, 2020, pp. 6246–6253.
- [31] K. Burnett, D. J. Yoon, Y. Wu, A. Z. Li, H. Zhang, S. Lu, J. Qian, W.-K. Tseng, A. Lambert, K. Y. Leung, *et al.*, "Boreas: A multi-season autonomous driving dataset," *The International Journal of Robotics Research*, vol. 42, no. 1-2, pp. 33–42, 2023.
- [32] H. Caesar, V. Bankiti, A. H. Lang, S. Vora, V. E. Liong, Q. Xu, A. Krishnan, Y. Pan, G. Baldan, and O. Beijbom, "nuScenes: A multimodal dataset for autonomous driving," in *Proceedings of the IEEE/CVF conference on computer vision and pattern recognition*, 2020, pp. 11 621–11 631.
- [33] J. Huai, B. Wang, Y. Zhuang, Y. Chen, Q. Li, and Y. Han, "SNAIL Radar: A large-scale diverse benchmark for evaluating 4D-radar-based slam," *The International Journal of Robotics Research*, vol. 44, no. 12, pp. 1941–1958, 2025.